ORIGINAL RESEARCH ARTICLE

Study on the Evolution Patterns of the Molten Pool and Inclusion Movement in Electron Beam Cold Hearth Melting Process

MEICHEN WANG, SHUANGJIE CHU, QIFEI ZHANG, GAOFEI LIANG, HAIYAN ZHAO, ZHENGFANG XU, YAOPING XU, XIAOLONG ZHU, YAMING SHI, and BO MAO

In order to deepen the understanding of the electron beam cold hearth melting (EBCHM) process in the production of titanium and its alloys, a thermal-fluid coupling model for the cold hearth refining process was established using ANSYS Fluent fluid simulation software. Comprehensive analysis was conducted on the molten pool morphology, temperature field, and flow field to investigate the influence of smelting process parameters on the mentioned aspects. Multi-physics equations were used to predict the migration behavior and residence time of inclusions in the molten pool, revealing that inclusions with low-density and near-matrix density have residence times exceeding 35 seconds, while high-density inclusions settle into the mushy zone within 20 seconds. The analysis of multi-particle inclusion movement behavior demonstrated a removal rate exceeding 93.1 pct for high-density inclusions, indicating excellent effectiveness. The simulation results showed satisfactory consistency with production experiments.

https://doi.org/10.1007/s11663-024-03393-8

I. INTRODUCTION

TITANIUM and its alloys possess outstanding properties such as high strength, corrosion resistance, and excellent biocompatibility, widely utilized in aerospace, marine engineering, and biomedical applications.[1–4] The control of high-quality titanium and its alloy ingot quality is crucial for subsequent processing steps, with vacuum arc remelting (VAR) and cold hearth melting (CHM) being the commonly used smelting methods in the titanium industry.[5] The VAR process involves a relatively small melting pool size, typically requiring 2-3 melts to ensure a uniformly distributed alloy composition for obtaining qualified ingots.[6] Meanwhile, the main advantage of CHM is the segregation of melting, refining, and solidification zones, which facilitates independent control over both energy input and the melting rate. The molten substance can stay in the cold hearth for an extended period, promoting the melting and homogeneous mixing of alloy elements. This enables obtaining uniformly composed ingots in one melt, thus achieving cost-effective production of titanium and its alloys.[7] CHM can be classified into two types based on the heat source: plasma arc cold hearth melting (PACHM) and electron beam cold hearth melting (EBCHM).[8,9] The PACHM furnace uses inert gas as the heat source medium,[10] yet the persistent issue of inert gas entering the ingot, leading to the formation of pores and surface segregation, remains unresolved,[11] Moreover, the high cost of inert gas significantly limits its industrial promotion. The EBCHM furnace functions under vacuum conditions, which efficiently eliminates volatile elements from the furnace chamber. Overall, EBCHM currently maintains a leading position in the production and application of titanium and its alloy ingots.[12]

The EBCHM process flow is illustrated in Figure 1, showing three stages: (1) Charging and Melting; (2) Molten pool Refining; (3) Solidification in the crystallizer. Initially, raw materials are transported to the

MEICHEN WANG, QIFEI ZHANG, and BO MAO are with the School of Materials Science and Engineering, Shanghai Jiao Tong University, Shanghai 200240, P.R. China. Contact e-mail: bmao@sjtu.edu.cn SHUANGJIE CHU is with the School of Materials Science and Engineering, Shanghai Jiao Tong University and also with the Baoshan Iron & Steel Co., Ltd., Shanghai 201900, P.R. China. Contact e-mail: sjchu@baosteel.com GAOFEI LIANG is with the Baowu Special Metallurgy Co., Ltd., Shanghai 200940, P.R. China. HAIYAN ZHAO and ZHENGFANG XU are with the School of Materials Science and Engineering, Shanghai Jiao Tong University and also with the Baowu Special Metallurgy Co., Ltd. YAOPING XU, XIAOLONG ZHU, and YAMING SHI are with the Yunnan Titanium Industry Co., Ltd., Chuxiong 651200, P.R. China.

Manuscript submitted May 18, 2024; accepted November 19, 2024.

Published online: 20 December 2024

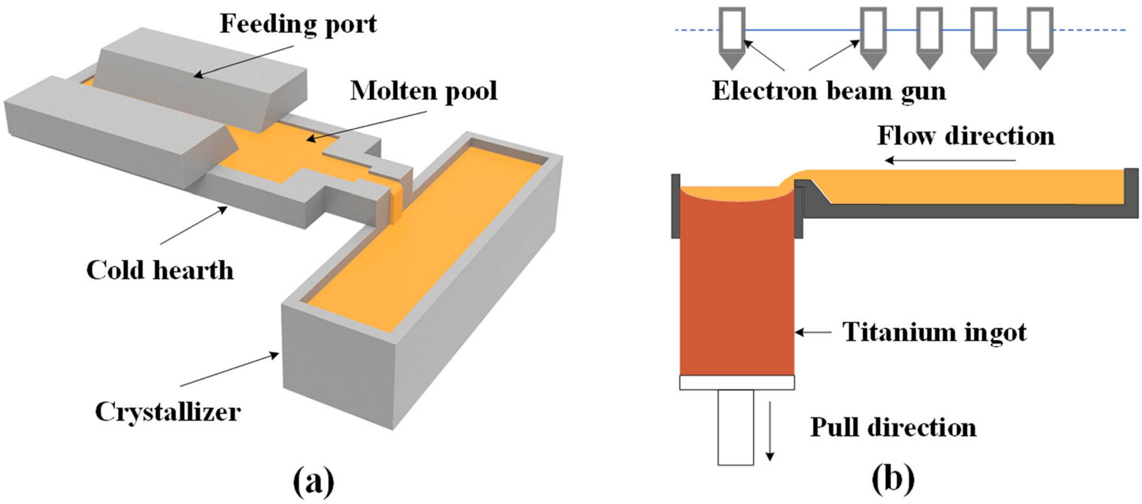

Fig. 1—Illustrates the schematic diagram of the EBCHM process.

charging port, melted under the high-energy impact of the electron beam, subsequently flowing into the cold hearth to form the molten pool. The residence time of the melt in the cold hearth can be autonomously controlled to complete the refining process, followed by flowing into the water-cooled crystallizer to solidify into ingots. Compared to the VAR process, which uses rod-shaped electrodes for feeding, the EBCHM process allows various feeding methods. One of the most crucial aspects is the recycling and remelting of titanium scrap, holding significant technical and economic value for achieving the recycling and regeneration of titanium materials.[13] Currently, titanium scrap primarily comes from smelting and processing processes, constituting internal industrial recycling. In contrast, the quantity of recycled material from external circulation, *i.e.*, scrapped consumer titanium products, is relatively small. However, with the future development of the titanium industry, the combined internal and external circulation of titanium scrap is expected to further promote the widespread adoption of the EBCHM process.[14] The EBCHM process has significant advantages in eliminating high-density inclusions (HDI) such as W, WC, and low-density inclusions (LDI) such as TiN.[15–17] Essentially, it employs density separation and melting mechanisms to eliminate HDI and LDI, respectively. HDI sinks to the bottom due to its significantly higher density than the titanium melt. The molten pool under the action of an electron beam can achieve a higher degree of overheating, facilitating the accelerated dissolution of LDI floating up to the surface of the molten pool.

The quality of ingots is crucial for subsequent processing of titanium components, leading many researchers to focus on the solidification process of ingots in studying EBCHM technology. For instance, Xu *et al.*[18] investigated the evolution of the internal molten pool in the crystallizer during the solidification process of Ti-0.3Mo-0.8Ni alloy ingots by establishing a three-dimensional non-steady-state model. They analyzed the influence of the internal molten pool within the crystallizer on casting quality from three aspects: fluid flow, temperature distribution, and solid-phase contour. Gao *et al.*[19] investigated the evaporation and segregation behavior of Al during the solidification process of EBCHM-cast ingots. They created a three-dimensional multiphysics field model to validate production data from the industry, uncovering the distribution trends of Al within the molten pool inside the crystallizer of Ti–6Al–4V alloy under various parameters. They proposed that reducing the pouring temperature is a promising solution for controlling segregation. Despite the robust development of EBCHM technology over the past decade, research regarding the EBCHM smelting process has been relatively scarce. Truong *et al.*[12] developed a numerical coupled heat flux model and employed four different electron beam scanning schemes based on it to study the evaporation of Al elements in the EBCHM process. They analyzed the temperature distribution and morphology of the molten pool under different scanning strategies.

In the long term, inclusions have been the main source of quality issues in titanium and its alloy components.[20–22] Inevitably, inclusions are introduced during the recycling and re-melting of titanium scrap, posing a challenge to the production of high-quality ingots. Although the EBCHM process is capable of removing LDI through buoyancy, evaporation, and dissolution, larger LDIs might not fully melt and could become sources of ingot defects as they flow into the ingot. Thus, even today, there is still a high demand to reduce the risk of inclusion contamination. Many researchers have studied the dissolution behavior of inclusions in titanium and its alloys. Bellot *et al.*[20] established a dissolution kinetics model for hard-alpha inclusions in titanium and its alloy melt, indicating that their dissolution process is controlled by the outward diffusion of nitrogen elements through the outer β phase into the melt. Related experiments[23,24] also suggest that the dissolution of hard-alpha inclusions occurs through the diffusion of nitrogen elements as a mediator into the melt. Ghazal *et al.*[25] conducted research on the dissolution behavior of HDI W and Mo, experimentally measuring the dissolution rates of W and Mo in titanium and its alloy melts. Relatively, there is a lack of research on the migration behavior of inclusions in the cold hearth of EBCHM processes. Bellot *et al.*[26] studied the movement trajectories of inclusions in the cold hearth molten pool. Their findings suggest that natural convection and Marangoni forces are the main factors influencing the migration of inclusions, where natural convection affects the migration of inclusions within the melt, while Marangoni forces influence their migration on the melt surface. In another study,[27] it was found that HDIs sink into a mushy zone at the bottom of the molten pool, while LDIs flow toward the sidewall of the cold hearth. When the density of inclusions exceeds a critical range, there is a significant probability of outflow from the cold hearth.

Previous research on the EBCHM process has made significant contributions, particularly in the in-depth investigation of ingot solidification. However, the refining process of the molten pool in the cold hearth has not received sufficient attention, and there is a lack of comprehensive numerical simulation work, especially in the systematic study of the migration behavior of inclusions in the molten pool. In this study, a thermal-fluid coupling model was established using ANSYS Fluent numerical simulation software. The evolution of the molten pool during the EBCHM process was investigated from the perspectives of molten pool morphology, temperature field, and flow field distribution. Detailed analysis was conducted on the migration trajectory, residence time, and removal rate of inclusions of different sizes and densities in the cold hearth. Experimental data from the industry validated the credibility of the model, demonstrating its potential in industrial applications.

II. MODELING APPROACH

A. *Governing Equations for the EBCHM Process*

The EBCHM process involves various physical and chemical phenomena such as heat transfer, fluid flow, and metal solidification. The heat supply to the melt comes from the continuous input of thermal energy from the high-temperature melt itself and energy input from the electron beam above the cold hearth. Thermal radiation of the melt, convective heat transfer in the environment, and heat exchange through the cold hearth are the main mechanisms of heat loss. The continuity equation of the mass conservation equation, based on the law of mass conservation, indicates that the mass flow rate within a unit volume remains constant. In the Eulerian description, the continuity equation can be expressed as a partial differential equation:

$$\frac{\partial \rho}{\partial t}+\frac{\partial(\rho v_x)}{\partial x}+\frac{\partial(\rho v_y)}{\partial y}+\frac{\partial(\rho v_z)}{\partial z}=0, \qquad [1]$$

where ρ represents the density of the material, t represents the fluid flow time, v_x , v_y, and v_z represent the time-averaged velocities in the x, y, and z directions, respectively.

In fluid dynamics, the law of energy conservation governs the transfer and transformation of energy within a fluid system, forming a fundamental equation for understanding fluid behavior and energy exchanges. In this research, the energy from the electron beam is applied to the melt from above to raise the domain's temperature. Simultaneously, heat in the domain is dissipated through the boundaries by conduction, convection, and radiation. Thus, the law of energy conservation is expressed as:

$$\frac{\partial}{\partial t}(\rho E)+\nabla\cdot(\vec{v}(\rho E+p))=\nabla\cdot\left(k_{\text{eff}}\nabla T-\sum_j h_j\vec{J}_j+(\tau_{\text{eff}}\cdot\vec{v})\right)+S_h, \qquad [2]$$

where k_{eff} refers to the effective thermal conductivity; $\vec{j}_j$ represents the diffusion flux of component j; the three terms on the right side account for energy transfer through heat conduction, material diffusion, and viscous dissipation; S_h is the volumetric heat source; E and h_j are functions related to the material's properties.

The law of momentum conservation is a fundamental equation for describing fluid motion and, when coupled with the Navier-Stokes equations, is used to explain complex fluid dynamics. The momentum conservation equation (in an inertial reference frame) can be written as:

$$\frac{\partial(\rho u_i)}{\partial t}+\frac{\partial(\rho u_i u_j)}{\partial x_j}=-\frac{\partial P}{\partial x_i}+\frac{\partial\left[\mu_{\text{eff}}\left(\partial u_i/\partial x_j+\partial u_j/\partial x_i\right)\right]}{\partial x_i}, \qquad [3]$$

Where u_i and u_j represent the time-averaged turbulent velocity in the i and j directions, where i, j = 1, 2, 3 correspond to the components of the melt flow velocity in the x, y, and z directions; P represents the pressure on the fluid element, and μ_{eff} is the effective turbulent viscosity coefficient.

As the molten material flows into the cold hearth, it solidifies into a solidified shell after water-cooled heat exchange. When the smelting reaches a steady state, there exist three phases in the cold hearth: the solid phase existing in the form of a solidified shell, the liquid phase in a molten state, and an intermediate mushy phase between the two, with their proportions no longer changing. During the solidification of the molten material, its enthalpy is represented by:

$$H=h+\Delta H=h_{ref}+\int_{T_{ref}}^{T}C_p dT, \qquad [4]$$

'where h represents sensible heat, ΔH is the latent heat; h_{ref} is the reference enthalpy, T_{ref} is the reference temperature, and C_p is the specific heat at constant pressure.

B. *Computational Domain and Boundary Conditions*

Raw materials such as sponge titanium are transported to the entrance of the cold hearth on a conveyor belt, melted into titanium liquid under the high-energy bombardment of electron beams, and then flow into the cold hearth under the influence of gravity. The domains of molten flow, solidification generating a solidified shell upon contact with the water-cooled wall, and the migration of inclusions are all within the cold hearth, as shown in Figure 2(a). A 1:1 three-dimensional model was constructed based on the physical dimensions of the EBCHM furnace at Panzhihua Yunti Industry Co., Ltd., measuring 1400 mm × 405 mm × 70 mm, as illustrated in Figure 2(b).

The numerical domain is divided into a hexahedral mesh with a unit size of 5 mm, totaling 384950 grid cells. To improve the efficiency of the simulation work, the flow field calculation is carried out first.[26] The SIMPLE algorithm is employed for pressure-velocity coupling, and the least squares method is used for gradient computation.[12] The discretization model for pressure is second-order, and momentum and energy use the second-order upwind scheme, while turbulent flow adopts the first order upwind scheme.[28] After the flow field calculation stabilizes, the Solidification & Melting model based on the enthalpy-porosity method in ANSYS Fluent is employed. The enthalpy-porosity method does not track specific liquid-solid boundaries but considers the mushy region during phase transition as a porous medium. The porosity of the region is equal to the volume fraction occupied by the liquid, and new liquid phase fractions are calculated in each iteration based on enthalpy equilibrium. In the fully solidified region, its porosity is zero, resulting in zero velocity in that region. To ensure computational stability and accuracy, we used an adaptive time step method, with an initial time step of 1e-5 seconds.

On the surface of the numerical domain, four regions are delineated, including the inlet region, the electron beam energy input region, the outlet region, and the water-cooled wall surface. The inlet is situated on both sides of the cold hearth, defined as a mass flow rate condition inlet. The numerical value of the mass flow rate is calculated based on the casting speed of the ingot, set at 800 kg/h for this computation, with a melt temperature of 2043 K. During the actual smelting process, there are 5 electron guns positioned above the furnace, operating within a power range of 120-250 kW. The electron beam energy input region is depicted in Figure 3(a). The impact of a single electron beam on the surface layer of the melt is illustrated in Figure 2(b), where Marangoni force accelerates the flow of the melt.[29] The energy transferred from the electron beam to the melt varies as the distance from the center of the electron beam to the surroundings changes. As per reference[8] thermal radiation of the melt accounts for 30 pct. The electron beam scans the surface of the molten pool in an orderly pattern at an ultra-high frequency, converting the energy of the electron beam into heat flux, expressed by the formula:

$$q_{\mathrm{EB}} = \frac{\eta_{\mathrm{EB}} P_{\mathrm{EB}}}{A}, \quad [5]$$

where η_{EB} stands for absorption rate, P_{EB} represents the electron beam power, and A denotes the area of the electron beam interaction zone.

Convection heat transfer occurs between the melt, solidified shell, and the cold hearth wall, according to the fundamental convective heat transfer equation:

$$q_{\mathrm{c}} = h_{\mathrm{wall}}(T_{\mathrm{m}} - T_{\mathrm{wall}}), \quad [6]$$

where T_{m} represents the temperature of the melt or the solidified shell, and T_{wall} represents the temperature of the cold hearth wall, which is assumed to remain constant at 300 K due to the effect of circulating cooling water. h_{wall} represents the interfacial heat transfer coefficient. According to literature,[8] when the melt first contacts the cold hearth wall, the interfacial heat transfer coefficient is 2000 W/m^2/K; As the melt begins to solidify and form a solidified shell, the interfacial heat transfer coefficient decreases to 1500 W/m^2/K. After the formation of the solidified shell, a gap is created between it and the cold hearth wall, resulting in an interfacial heat transfer coefficient of 425 W/m^2/K. Hence, the actual interfacial heat transfer coefficient fluctuates within a range of values. This paper defines the interfacial heat transfer coefficient using a functional approach, stabilizing at 425 W/m^2/K when the molten pool approaches a steady state.

C. *Material Properties*

The phase transitions and melting processes in the solid state have a major impact on the thermophysical properties of titanium and its alloys. Previous research often used fixed values for certain critical parameters of

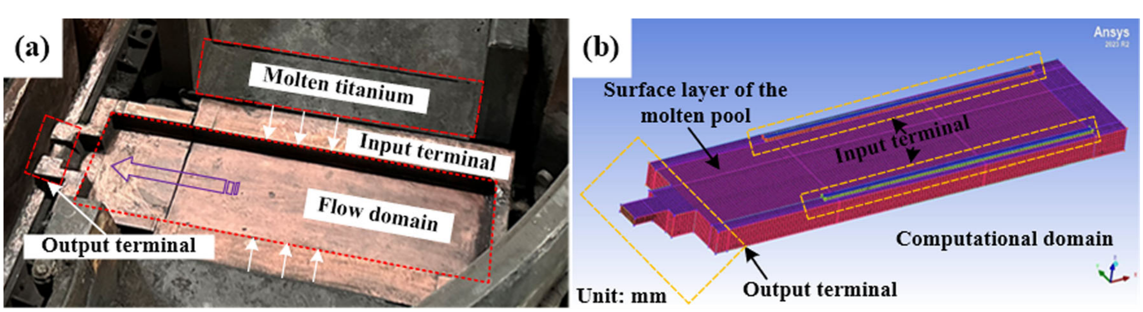

Fig. 2—EBCHM furnace (*a*) and numerical domain (*b*).

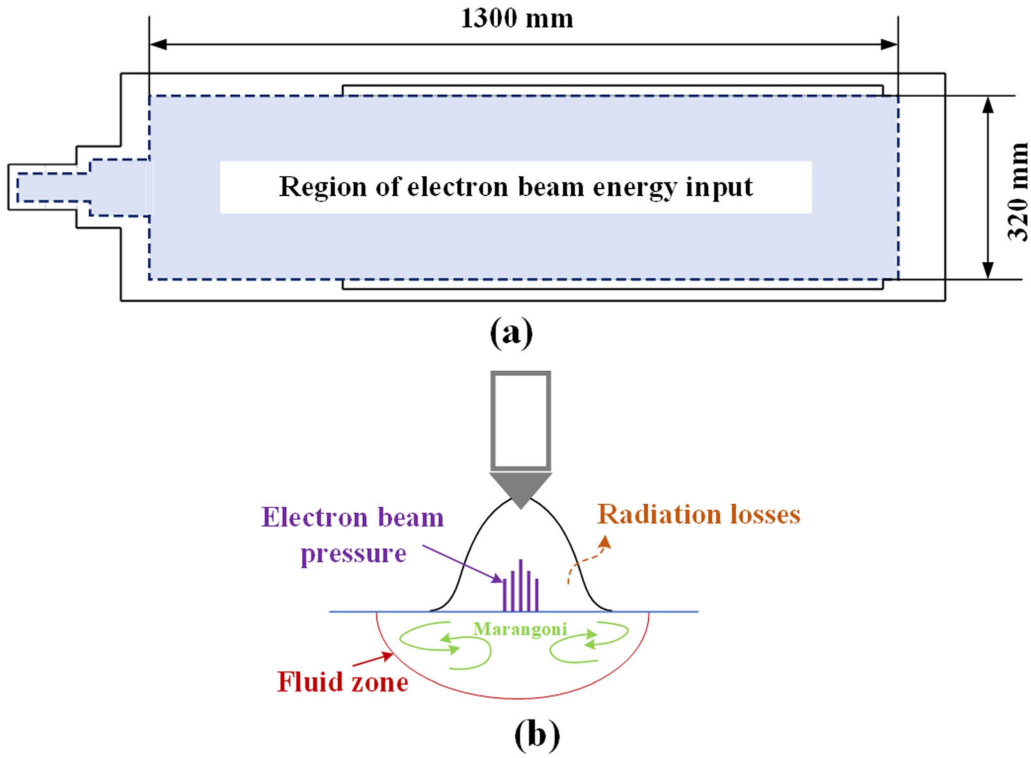

Fig. 3—Electron beam energy input region (*a*) and the effect of a single electron beam on the surface of the molten pool (*b*).

the materials studied, which could potentially compromise the accuracy of the simulation results. For Ti–6Al–4V in this study, the thermal physical properties related parameters were computed using two software, ProCAST and JMatPro. As illustrated in Figure 4, density, thermal conductivity, specific heat, and dynamic viscosity are functions of temperature, and these parameters were imported into the ANSYS Fluent case using User Defined Functions (UDFs). The Liquidus temperature and Solidus temperature influence the morphology of the pasty zone, being 1931 K and 1758 K, respectively.

D. *Inclusion Movement*

In this paper, one of the research focuses is on inclusions, which are classified into different categories according to their size and density. According to the research of relevant scholars,[20,27,30] the inclusions are simplified as spheres, with common diameters ranging from several tens to several hundreds of microns. As a result, the diameters of inclusions in this study are divided into three levels: 30, 100, and 300 μm. Given that the density of the Ti–6Al–4V alloy melt is around 4450 kg/m^3, the inclusion density levels were set at 3500, 4000, 4500, and 5000 kg/m^3, as illustrated in Figure 5(a). The Discrete Phase Model (DPM) is employed to calculate the migration trajectory of inclusions in the cold hearth, with the settings of the Particle Random Tracking Model and Particle Clustering Release Method as 'standard'. Given the small size of the inclusion particles, it is assumed that the continuous phase (liquid) affects the motion of the dispersed phase (solid), while the dispersed phase does not influence the continuous phase. Furthermore, collisions, agglomeration, and fragmentation of inclusions during their movement are disregarded.

Within the molten pool, inclusions experience the collective impact of gravity, buoyancy, thermophoretic force, drag force, virtual mass force, Saffman lift force, and pressure gradient force,[31,32] as depicted in Figure 5(b).

The equation governing the movement of inclusions within the melt is expressed as:

$$\rho_P \frac{\pi}{6} d_P^3 \frac{dv_P}{dt} = F, \qquad [7]$$

where ρ_p, d_p, and v_P represent the density, particle size, and velocity of the inclusions, respectively. F denotes the resultant force of the mentioned forces.

The thermophoretic force on the inclusions in the melt is caused by the temperature gradient, leading to the movement of inclusions in a non-uniform temperature field. Its direction and magnitude depend on both the temperature gradient and the characteristics of the inclusions. Its expression is as follows:

$$F_t = -k_{\mathrm{thermo}} \cdot \nabla T, \qquad [8]$$

where k_{thermo} represents the thermophoretic coefficient, describing the responsiveness of inclusions to temperature gradients. ∇T denotes the temperature gradient, indicating the rate of temperature change with space.

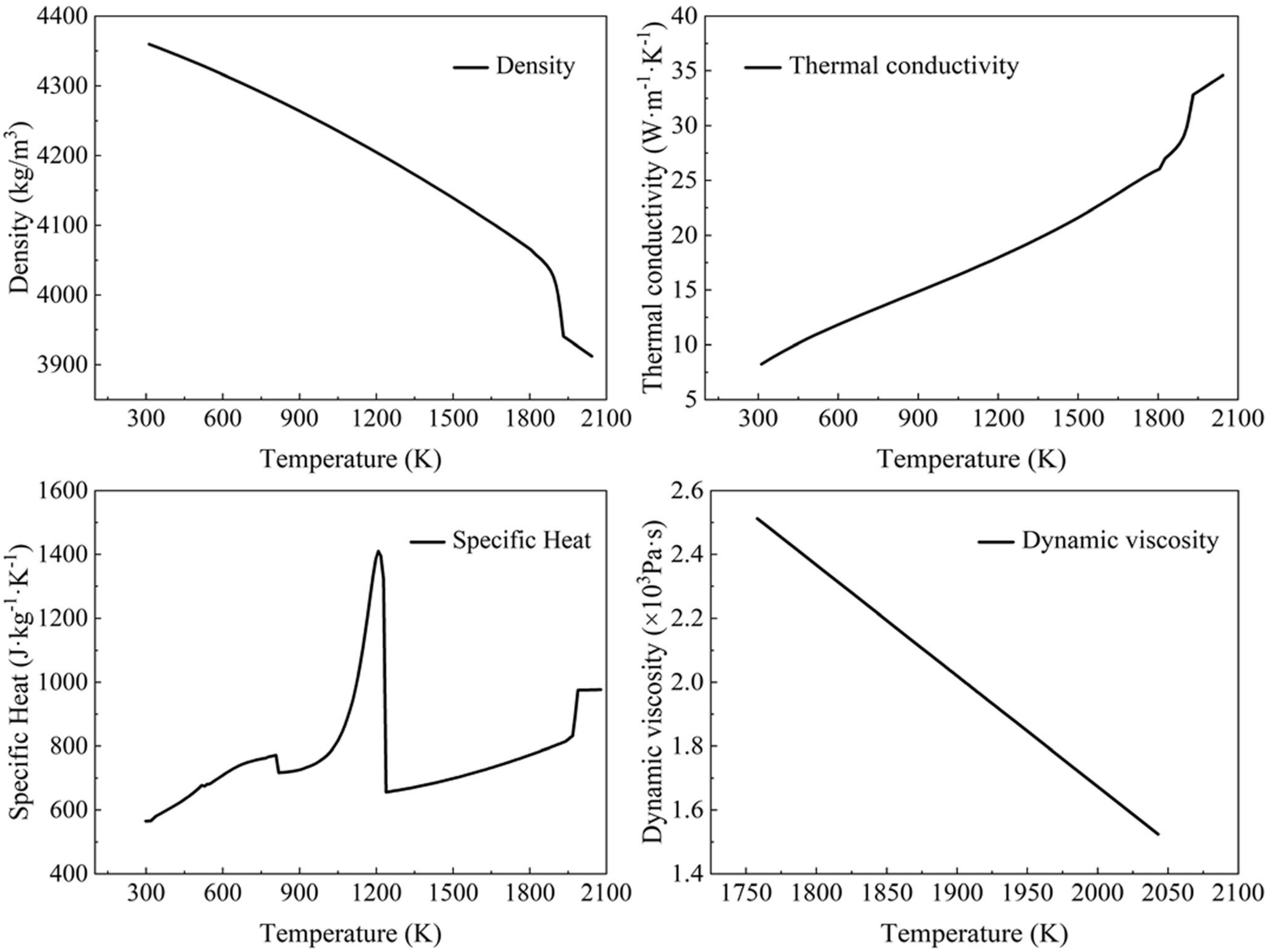

Fig. 4—Parameters related to thermophysical properties of Ti–6Al–4V.

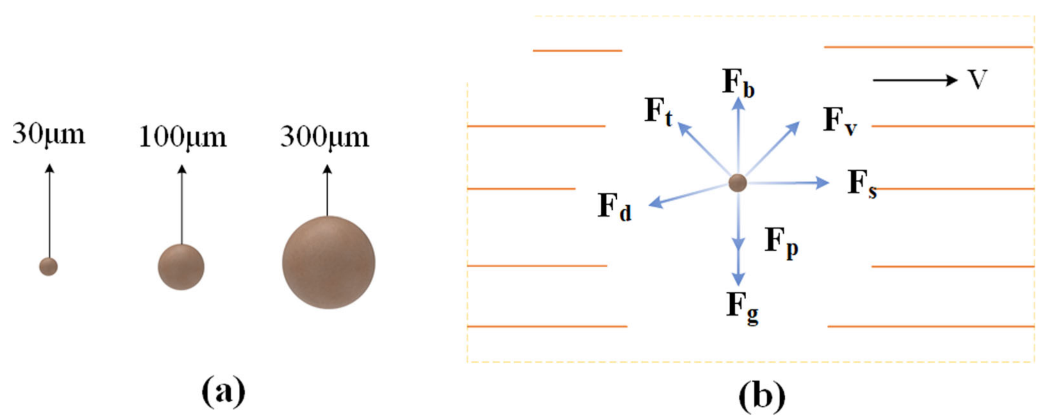

Fig. 5—Inclusion levels (*a*) and force analysis of inclusion movement in the melt (*b*).

The drag force is caused by the viscosity of the melt, exerting a force on the inclusions due to the melt flow, attempting to move or carry them into the flow region, thereby disrupting the trajectory of the inclusions. Its expression is as follows:

$$F_{\mathrm{d}} = C_{\mathrm{D}} \frac{3}{4} \frac{v_{\mathrm{m}}}{\rho_{\mathrm{p}} d_{\mathrm{p}}^{2}} Re_{\mathrm{p}} \left(v_{\mathrm{m}} - v_{\mathrm{p}} \right), \quad [9]$$

where C_{D} represents the drag force coefficient, v_{m} stands for the melt velocity, and Re_{p} denotes the

Reynolds number of the melt adhering to the surface of the inclusions.

The virtual mass force describes the extra resistance experienced by inclusions during their movement within the melt, aiding to more precisely predict the impact on the movement of inclusions within the melt. Its expression is as follows:

$$F_{\mathrm{v}} = C_{\mathrm{v}} \frac{\rho_{\mathrm{m}}}{2\rho_{\mathrm{p}}} \frac{d(v_{\mathrm{m}} - v_{\mathrm{p}})}{dt}, \quad [10]$$

where C_{v} represents the virtual mass force coefficient.

The Saffman lift force is commonly employed to describe the movement of inclusions within a melt, especially in high Reynolds number flows, such as inclusions suspended within a melt. It arises from the shear and turbulence effects in the melt and is typically generated around vortices or turbulent regions. Its expression is as follows:

$$F_{\mathrm{s}} = C_{\mathrm{s}} \frac{6K_{\mathrm{s}}u_{\mathrm{eff}}}{\rho_{\mathrm{p}}\pi d_{\mathrm{p}}} \left(\frac{\rho_{\mathrm{m}}\xi}{u_{\mathrm{eff}}}\right)^{1/2} (v_{\mathrm{m}} - v_{\mathrm{p}}), \quad [11]$$

where C_{s} represents the correction coefficient for the Saffman lift force, K_{s} represents the coefficient for the Saffman lift force, and ξ indicates the gradient of the melt velocity in a specific vertical direction.

The Pressure gradient force refers to the force acting on internal inclusions in the melt when there is a pressure gradient. This force drives inclusions from high-pressure areas to low-pressure areas, representing one of the significant driving forces for the migration of inclusions. Its expression is as follows:

$$F_{\mathrm{p}} = \frac{\rho_m}{\rho_{\mathrm{p}}} \frac{dv_m}{dt} \quad [12]$$

Inclusions primarily originate from the raw materials and are carried into the cold hearth along with the melt. The inlet velocity of these inclusions corresponds to that of the melt, adhering to the escape condition. The cold hearth walls are modeled as slip walls, meaning that inclusions rebound upon contact without being absorbed. When inclusions reach the exit position, they escape and proceed to the next smelting stage, again following the escape condition. In regions where the solid-liquid phase is stable, the interface is treated as a trap condition, assuming that inclusions entering the mushy zone encounter resistance and are adsorbed. The inclusion removal rate is calculated based on the simulation results of the DPM model, and the expression is as follows:

$$T_{\mathrm{a}}\mathrm{pct} = \frac{N_{\mathrm{trap}}}{N_{\mathrm{in}}} \times 100, \quad [13]$$

where N_{trap} represents the captured quantity of inclusions, and N_{in} represents the quantity of inclusions at the inlet.

III. RESULTS AND DISCUSSION

A. *Multiphysics Coupling Results*

In the EBCHM process, the titanium and its alloy melt form a solidified shell upon contacting and exchanging heat with the cold hearth. When the size of the solidified shell remains relatively constant, the distribution of the solid phase, mushy zone, and liquid phase within the melt stabilizes, as illustrated in Figure 6(c). Figure 6(a) displays a transverse slice 450 mm away from the tail end of the cold hearth, providing insights into the melt's morphological characteristics by analyzing its simulated results. In Figure 6(b), a phase distribution diagram transitions from blue to red, indicating a continuous increase in the liquid phase volume. Specific colors correspond to the numerical values of the liquid phase volume as per the scale. Regions labeled I, II, and III in Figure 6(b), respectively, represent the liquid phase zone, mushy zone, and solid phase zone. The upper liquid phase and the middle mushy zone are roughly separated by the liquidus line; similarly, the mushy zone and the lower solid phase are roughly divided by the solidus line. Figures 6(d) and (e) depict the temperature and density distributions within

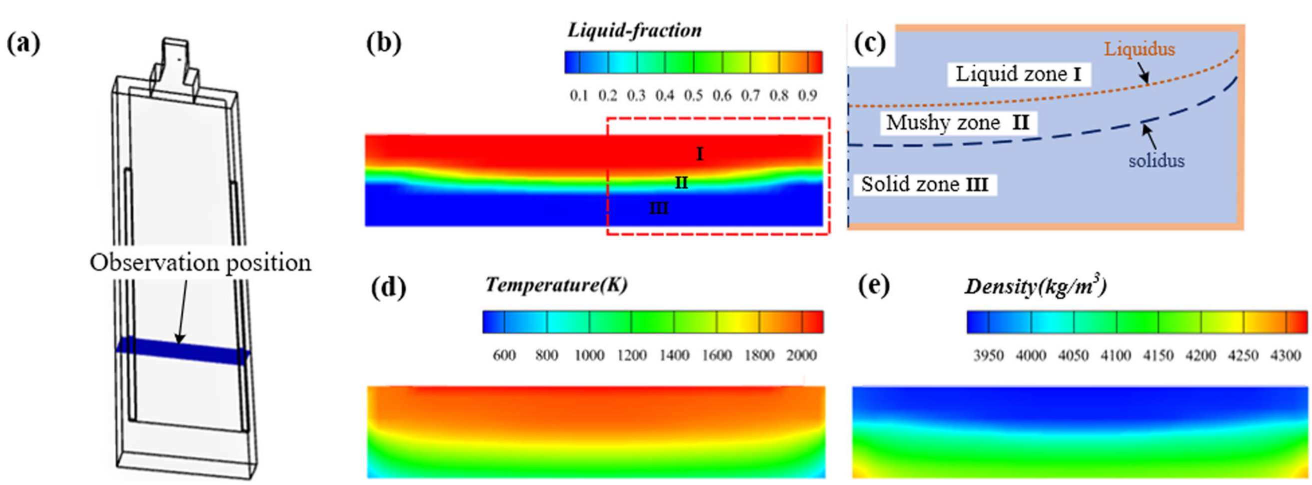

Fig. 6—Characteristics of the melt in the cold hearth cross-section.

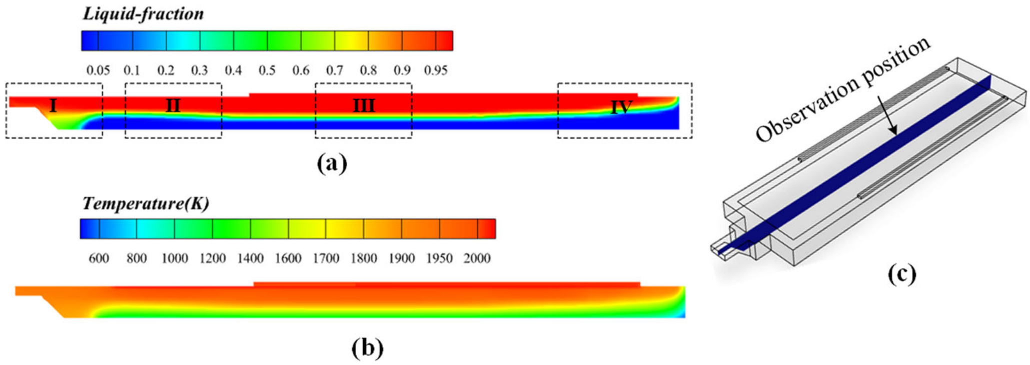

Fig. 7—Vertical section of cold hearth molten pool morphology.

the melt, where the upper layer of the melt exhibits a temperature exceeding 2000 K, and its density is below 3950 kg/m^3. Consequently, impurities with densities lower than this value can more easily float to the surface, facilitated by the higher temperature, which accelerates their dissolution. The flow of the melt is impeded within the mushy zone, where the density of the melt is approximately 4150 kg/m^3. In the event high-density impurities enter the mushy zone under the influence of gravity, they will be captured. Hence, the evolutionary patterns in melt morphology significantly impact the removal of inclusions.

Figures 7(a) and (b) represent phase distribution and temperature distribution, respectively. They are observed at the longitudinal section illustrated in Figure 7(c), aiming to analyze the longitudinal morphology of the EBCHM furnace molten pool. In Figure 7(a), areas I, II, III, and IV are located at the overflow outlet, near the entrance, middle section, and tail of the cold hearth. The distribution of liquid zone, mushy zone, and solid zone varies across these regions. As the overflow outlet area of the cold hearth, Zone I is filled with fast-flowing melt, with significantly higher scouring intensity of the melt on the mushy zone beneath the cold hearth compared to other locations, as also indicated in Figure 7(b) by the notably higher temperature of the bottom melt at the overflow outlet. Therefore, there is no stable solid phase in the overflow outlet area, instead, it is replaced by a mushy zone. The distribution of the three-phase regions in Zones II and III is similar, vertically consisting of nearly half proportions of the liquid phase, mushy zone, and solid phase. In Zone II, the liquid phase proportion is 47.7 pct, lower than the 53.4 pct in Zone III. This is due to Zone III being located at the melt inlet, where the melt possesses higher kinetic energy and scour the mushy zone, resulting in a lower height of the solid phase in Zone III compared to Zone II. It is worth noting that the mushy zone thickness in Zones II and III is quite similar, mainly due to the influence of the liquid-solid phase line attributes of the metal melt. Zone IV, as the tail end of the cold hearth, is affected by water-cooling on three sides, exhibiting a significantly higher proportion of the solid phase compared to the other four zones, with the height of the solidified shell increasing as it gets closer to the tail end.

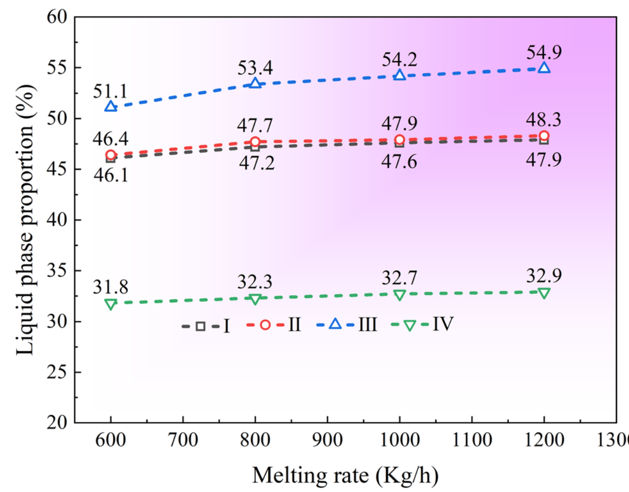

Fig. 8—Influence of melting rate on the liquid phase proportion.

Considering the practical manufacturing process, the smelting rate is adjusted according to production plans. Four common smelting rates (600/800/1000/1200 kg/h) were selected for simulation calculations. When the melting pool reaches a stable state, the liquid phase proportion was measured, selecting regions I, II, III, and IV from Figure 7(a) as measurement positions. The measurement results in Figure 8 show that with an increase in the smelting rate, the liquid phase proportions in the four regions have all increased. At 1200 kg/h compared to 600 kg/h, the liquid phase proportions in positions I, II, III, and IV increased by 3.9, 4.09, 7.43, and 3.45 pct, respectively. The marginal increases suggest a minor impact of the smelting rate on the morphology of the melting pool. This could be attributed to the predominant influence of the cold bed's cooling effect on the solidification morphology. Hence, in practical production, a relatively broad range of smelting rates can be set.

To compare with simulation results, dissected analysis of the solidified shell after the completion of EBCHM process was conducted. Ti–6Al–4V alloy was used as the experimental material with an average melting rate of 800 kg/h, resulting in a solidified shell as shown in Figure 7(a). The measurements for the length and width of the solidified shell were 1410 and 398 mm, respectively, exhibiting an error within 1.7 pct when compared to the simulation results. The upper layer of Figure 9(b) presents numerical simulation results, where the blue area represents the solid phase, corresponding closely to the appearance of the solidified shell in the lower part of the figure. Measurements were conducted for the thickness of the solidified shell at the end of the cold hearth, as shown in Figure 9(c), indicating a depth of 80 mm. The phase proportion distribution graph is consistent with the actual measurement results, and the trend of the solid-liquid phase boundary is closely aligned. Considering the wear that occurs when the solidified shell is removed from the cold hearth, the simulation results exhibit a high level of credibility, demonstrating its potential in guiding EBCHM actual production.

B. *Flow Field Distribution*

From a macro perspective, the flow behavior of titanium alloy melt in the cold hearth is driven by three main contributors: convective flow of the melt from high-temperature zones to low-temperature zones, Marangoni shear stress on the melt surface due to the electron beam heat source, and local turbulence induced by the descent of the melt from the inlet. Figure 10 displays the velocity contour map, velocity vector map, and the position of the observation area in the horizontal plane of the surface melt within the cold hearth. The area near the inlet is chosen for observation due to the high kinetic energy of the melt, creating vortices within it. This causes fluid micro-elements to move erratically in various directions aside from the main flow, resulting in localized turbulence. Hence, the flow field distribution near the inlet is the most intricate and significantly impacts the migration path of inclusions.

Based on the velocity contour map, the observation area can be divided into low, medium, and high-speed regions. The inlet area represents the low-speed region (0.01~0.03 m/s) due to the nearly vertical descent of molten titanium liquid into the cold hearth, resulting in a smaller horizontal velocity component. Observing the velocity vector maps in zones I and II, the fluid near the inlet shows a trend of flowing towards the inlet, especially more pronounced at both ends of the inlet's narrow side. The melt at the inlet falls nearly vertically, creating troughs in the calm surface melt, which exerts attraction on nearby melt. Consequently, inclusions fall with the melt, exhibiting a state of medium-range disordered motion at the inlet. The medium-speed region (0.03~0.09 m/s) spans from the inlet to the center of the cold hearth and the outer areas at both ends of the narrow side of the inlet. The horizontal velocity component of the melt between the inlet and the cold hearth's center mainly originates from turbulent disturbances and Marangoni shear stress, illustrated in Figure 3(b). The outer regions at both ends of the narrow side of the inlet experience more influence from thermal convection, particularly near the rear of the cold hearth. The velocity vector map in Zone II indicates the flow of high-temperature melt from the center of the cold hearth towards the tail end, aligning with the analysis in Section III–A. If low-density inclusions accompany the melt to the tail region, they are likely to remain there for an extended period, potentially enhancing inclusion removal rates. The high-speed region (0.09~0.113 m/s) extends from the inlet to the cold hearth wall, and due to the hindrance posed by the wall, the fluid's movement is obstructed, resulting in higher melt velocities within this confined area. The velocity vector map illustrates velocity components directed almost perpendicular to the wall, with the maximum velocity reaching 0.113 m/s. The existence of this region intensifies the turbulence near the inlet and complicates the migration trajectory of inclusions.

High-energy-density electron beams impact the surface of the melt, while the lower part of the melt exchanges heat with the cold hearth, resulting in a significant vertical temperature gradient within the melt. The thermal convection driven by this gradient effectively stirs the melt, leading to a nearly uniform distribution of elemental composition within the melt. In Figure 11, the central symmetric plane along the length direction of the cold hearth is selected as the observation surface, displaying velocity contour and velocity vector maps of the melt's vertical flow on this surface. Considering the analysis in Section III–A, a solidified shell forms at the bottom of the melt, where the flow velocity in the solid phase and mushy zone is below 0.01 m/s. The velocity vector maps of zones I and II also indicate minimal movement at the bottom of the melt. Compared with Fig. 7(a), it is evident that the internal velocity in the liquid phase region is not uniform. Only the surface melt maintains a high-speed flow, while the liquid phase below the surface has a lower flow rate. If high-density inclusions enter the low-speed area, they will have a hard time escaping and are likely to be captured in the mushy zone. The velocity range of the surface melt is 0.03~0.09 m/s. When observing region I, the melt near the exit not only

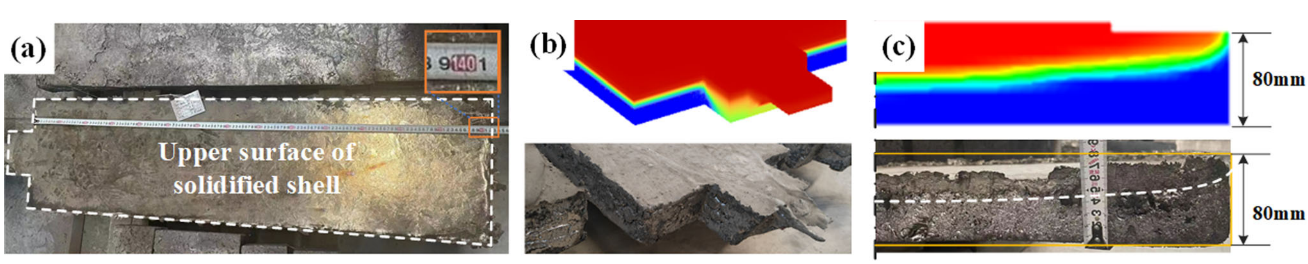

Fig. 9—Comparison of experimental and simulated solidified shell morphologies.

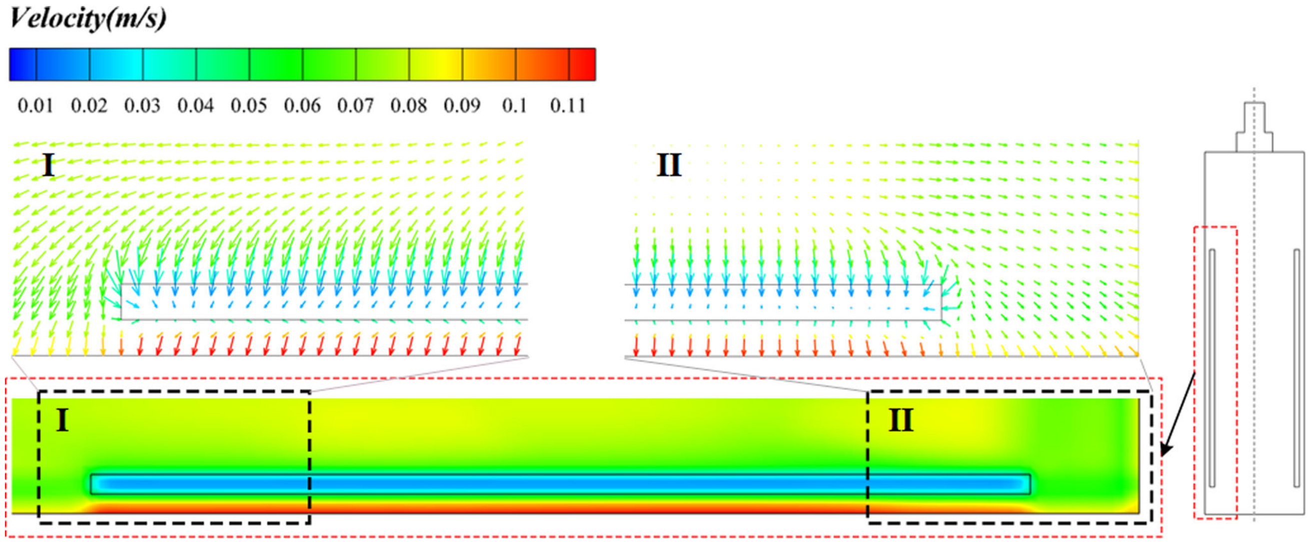

Fig. 10—Horizontal flow distribution at the inlet of the cold hearth in plane.

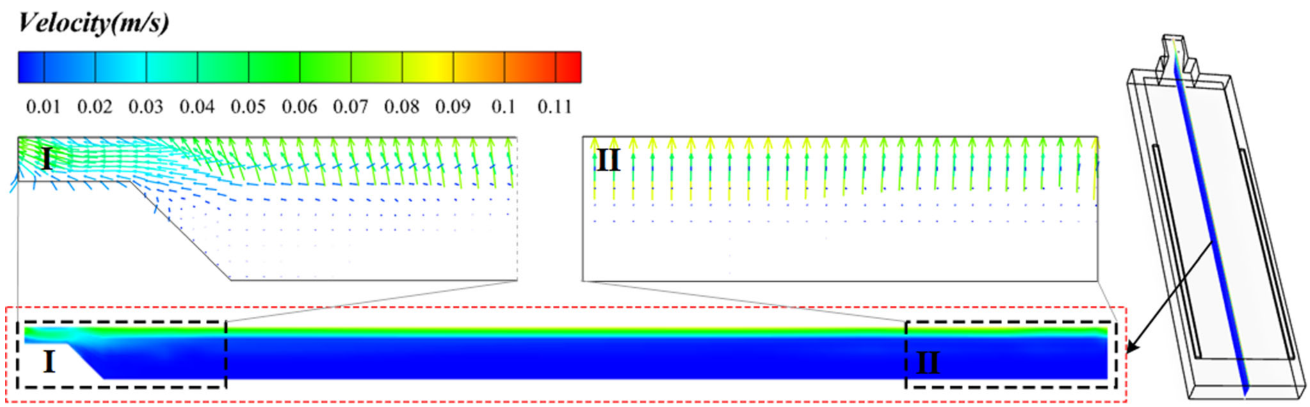

Fig. 11—Flow field distribution along the longitudinal central symmetry plane in the cold hearth.

exhibits the main upward vertical flow as in region II but also shows a horizontal velocity component offset towards the outlet. The closer to the inlet, the more straight the melt velocity vectors become. In case inclusions enter this region, there is a high probability that they will overflow with the melt from the outlet into the crystallizer, reducing the quality of the ingot.

C. *Movement of Inclusions in EBCHM Process*

To specifically analyze the migration trajectory and residence time of inclusions in the cold hearth, single-particle inclusions were chosen as the research subject. Figure 12 depicts the movement trajectory of low and high-density single-particle inclusions in the melt pool, with trajectory color representing the residence time of inclusions in the melt pool. The deep blue and deep red colors, respectively, indicate the initial and final stages of inclusion residence. The initial trajectories of low and high-density inclusions entering the melt pool from the geometric center of the inlet are identical, moving deeper into the melt pool along with the inlet melt, consistent with the analysis in Section III–B. The low-density inclusion (3500 kg/m^3) begins to rise in the center of the melt pool and migrates towards the outlet, driven by the vertical velocity component mentioned in Figure 10. This inclusion resides in the melt pool for 36.2 seconds, as shown in Figure 8(a). The high-density inclusion (5000 kg/m^3), primarily influenced by gravity, moves within the melt pool, eventually settling in the mushy zone after 11.4 seconds of migration into the deeper regions.

Building upon the previous study, a comparative analysis of the residence times of inclusions with varying densities and diameters within the cold hearth was conducted. To enhance data accuracy, each simulation was run three times, and the residence time was averaged, as illustrated in Figure 13. For clarity, inclusions with a density of 3500 kg/m^3 and a diameter of 30 μm are denoted as 3500-30, following similar shorthand for other inclusions. Based on the titanium alloy melt density variation with temperature in Figure 4,

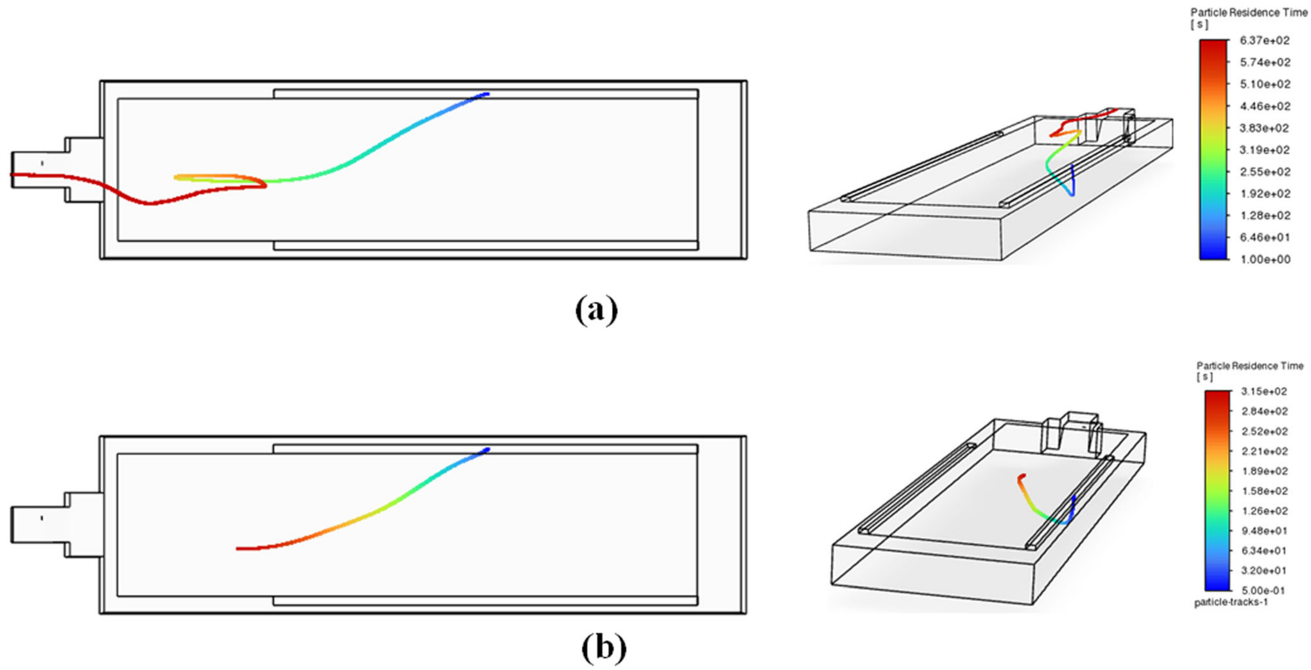

Fig. 12—Migration trajectory and residence time of single-particle inclusion: (*a*) 3500 kg/m^3; (*b*) 5000 kg/m^3.

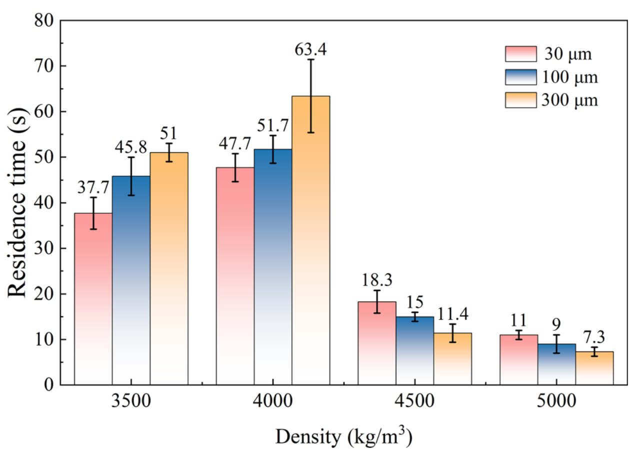

Fig. 13—Comparison of residence times for inclusions with different densities and diameters in the cold hearth.

inclusions of different densities were categorized: 3500, 4000, 4500, and 5000 kg/m^3 representing low-density, near-matrix density, and high-density inclusions, respectively. There is a significant difference in the residence time of inclusions in the cold hearth, with the 4000-300 inclusion having the longest residence time of 63.4 seconds, while the 5000-300 inclusion has the shortest residence time at 7.3 seconds, a nearly 9-fold difference. In low-density and close-to-matrix density inclusions, larger sizes correspond to longer residence times and more complex migration trajectories. Conversely, larger sizes of high-density inclusions exhibit shorter residence times, such as the 5000-300 inclusion with a residence time of only 7.3 seconds. Both low-density and close-to-matrix density inclusions have a residence time in the melt exceeding 35 seconds, with the residence time of close-to-matrix density inclusions longer than that of low-density inclusions. This could be due to the quicker ascension of low-density inclusions upon entering the melt. As per the analysis in Section III–B, the closer the molten material is to the upper layer, the higher its flow rate, thus resulting in faster flow for low-density inclusions and shorter residence times. It's noteworthy that both low-density and close-to-matrix density inclusions have flown out through the overflow outlet, indicating that these two density inclusions, if not entirely dissolved under the high-temperature bombardment of the electron beam, will enter the ingot along with the melt, potentially causing quality issues. In comparison, the residence time of high-density inclusions is within 19 seconds, with the 5000 kg/m^3 inclusions entering the mushy zone around 10 seconds, ceasing their migration trajectories, which confirms the effective removal of high-density inclusions by the EBCHM process.

Multiple particulate inclusions are uniformly introduced at the inlet, as depicted in Figure 14(a). Analysis is conducted on the migration behavior and removal efficiency of these inclusions within the molten pool. The interface at a liquid phase proportion of 0.4 is set as the adsorption boundary, shown in Figure 14(b), where inclusions residing in this area or in regions with a lower liquid phase proportion for over 5 seconds are considered captured. In Figure 14(c), from top to bottom, the positions where the particles of inclusions 4500-30, 4500-300, and 5000-300 finally settle in the cold hearth are shown. It can be observed that the inclusions of 4500-30 are relatively evenly distributed across the cold hearth, while those of 5000-300 are captured near the

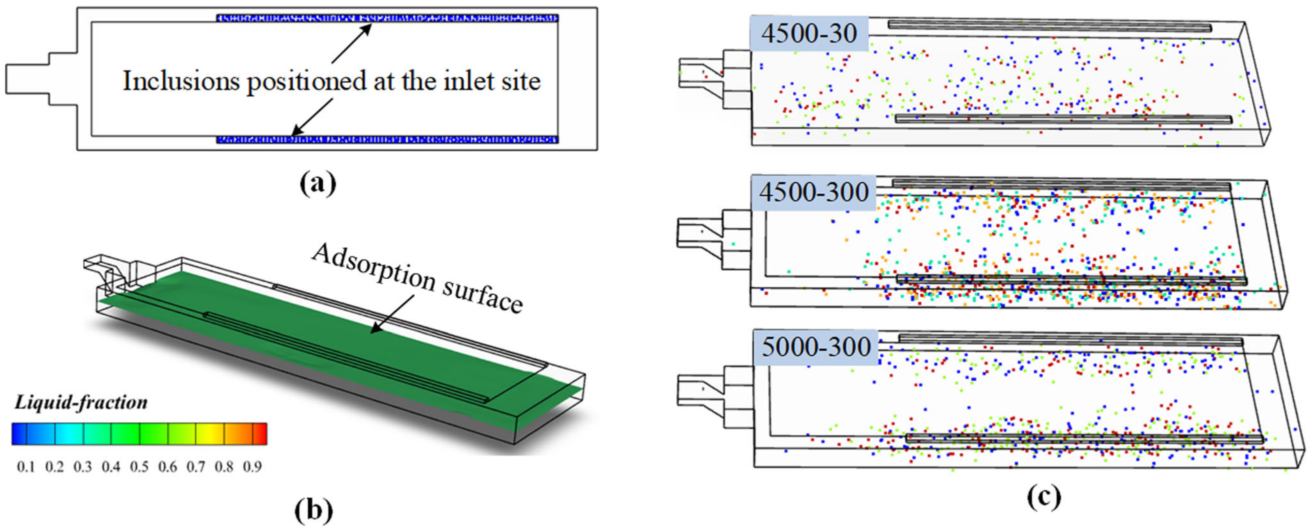

Fig. 14—Distribution of multiple inclusions in the cold hearth.

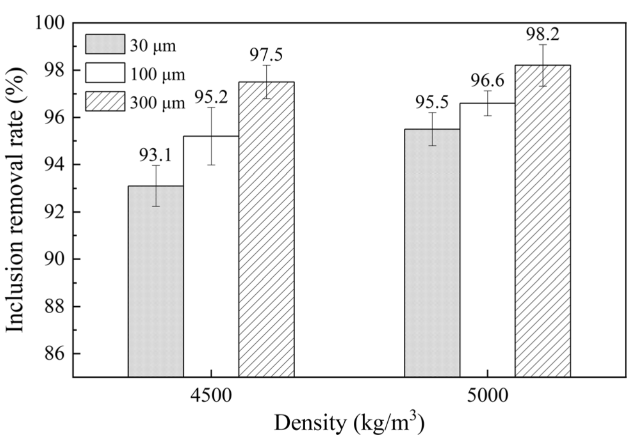

Fig. 15—Removal rate of multiple particulate inclusions in the cold hearth.

entrance, and the distribution of 4500-300 falls between the two case. To further investigate the removal efficiency of high-density inclusions in EBCHM, inclusions with densities of 4500 and 5000 kg/m^3 and diameters of 30, 100, and 300 μm were selected for orthogonal simulation experiments. The experiments were repeated three times, and the average values were taken as the removal rates, as shown in Figure 15. The removal rate of 4500-30 inclusions was the lowest but still reached 93.1 pct, while the removal rate of 5000-300 inclusions was the highest at 98.2 pct. The removal rate of inclusions increased with higher density. For inclusions with diameters of 30, 100, and 300 μm at a density of 5000 kg/m^3, the removal rates increased by 2.4, 1.4, and 0.7 pct, respectively, compared to inclusions at 4500 kg/m^3 density. Increasing the particle size also moderately increased the removal rate of inclusions. It's important to note that in this simulation process, the initial concentration of multi-particle inclusions in the cold hearth was set higher than in actual industrial production. This was done to better understand the behavior of multiple inclusions in the cold hearth. Adhering to the inclusion concentrations used in industrial production would likely further enhance the removal rate. Overall, the simulation results confirm the significant advantage of EBCHM in removing high-density inclusions.

IV. CONCLUSIONS

In this study, a thermal-fluid coupled CFD model was developed using ANSYS Fluent numerical simulation software, successfully simulating the refining process of the molten pool in the EBCHM process within the cold hearth. A comprehensive analysis was conducted on the molten pool morphology, temperature field, flow field, and inclusion movement. Industrial experimental data validated the viability and cost-effectiveness of the mathematical simulation method employed for studying the EBCHM process. The research findings are as follows:

1. At the stable state of the molten pool, it consists of a liquid zone, a mushy zone, and a solid phase zone from top to bottom, with the liquid phase occupying approximately 50 pct. The influence of the smelting rate on the molten pool's morphology is minimal, allowing for a wide adjustable range in actual production. The morphology of the solidified shell affects the flow of the melt and the migration of inclusions. Simulation results align with actual experimental measurements, showcasing the potential of simulations in guiding real production processes.
2. Convection flow, Marangoni effect, and local turbulence are the primary factors driving the molten pool flow. The flow state of the melt in different velocity regions significantly influences the removal of inclusions and their migration paths. The flow field distribution of the melt at the inlet is the most complex, with flow velocities of the melt in the solid phase and

mushy zone at the bottom of the melt being below 0.01 m/s.

3. Simulating the movement trajectories and residence times of inclusions in the molten pool revealed significant differences in the residence times of inclusions with different densities and diameters within the cold hearth. Low-density and near-matrix density inclusions stayed for over 35 seconds, while high-density inclusions remained for less than 20 seconds. The simulation results for multiple-grain inclusions demonstrate that EBCHM processes achieve a removal rate of over 93.1 pct for high-density inclusions, exhibiting outstanding removal efficiency.

ACKNOWLEDGMENTS

The authors acknowledge with gratitude funding received from the National Key R&D Program of China (No. 2022YFB3705602) and Scientific Research Plan Project of Shanghai, P.R. China (No. 22SQBS00600). The authors are grateful for the Instrumental Analysis Center in Shanghai Jiao Tong University.

CONFLICT OF INTEREST

On behalf of all authors, the corresponding author states that there is no conflict of interest.

REFERENCES

1. D. Banerjee and J.C. Williams: *Acta Mater.*, 2013, vol. 61, pp. 844–79.
2. Q. Zhao, Q. Sun, S. Xin, Y. Chen, Wu. Cong, H. Wang, Xu. Jianwei, M. Wan, W. Zeng, and Y. Zhao: *Mater. Sci. Eng. A*, 2022, vol. 845, p. 143260.
3. A. Biesiekierski, J. Wang, M.A.-H. Gerpreel, and C. Wen: *Acta Biomater.*, 2012, vol. 8, pp. 1661–69.
4. Y.-Y. Zong, S.-H. Huang, G. Bin, and D.-B. Shan: *Trans. Nonferrous Metals Soc. China*, 2015, vol. 25, pp. 2901–11.
5. C. Cui, Hu. BaoMin, L. Zhao, and S. Liu: *Mater. Des.*, 2011, vol. 32, pp. 1684–91.
6. C.R. Woodside, P.E. King, and C. Nordlund: *Metall. Mater. Trans. B*, 2013, vol. 44B, pp. 154–65.
7. Q. Liu, X. Li, and Y. Jiang: *Vacuum*, 2017, vol. 141, pp. 1–9.
8. J.-P. Bellot, L. Décultot, A. Jardy, S. Hans, E. Doridot, J. Delfosse, and N. McDonald: *Metall. Mater. Trans. B*, 2020, vol. 51B, pp. 1329–38.
9. V. Güther, M. Allen, J. Klose, and H. Clemens: *Intermetallics*, 2018, vol. 103, pp. 12–22.
10. S. Ji, J. Duan, L. Yao, D.M. Maijer, S.L. Cockcroft, D. Fiore, and D.W. Tripp: *Int. J. Heat Mass Transf.*, 2018, vol. 119, pp. 271–81.
11. J.C. Williams and R.R. Boyer: *Metals*, 2020, vol. 10, p. 705.
12. V.-D. Truong, Y.-T. Hyun, J.W. Won, W. Lee, and J. Yoon: *Materials*, 2022, vol. 15, p. 820.
13. O. Takeda and T.H. Okabe: *JOM*, 2019, vol. 71, pp. 1981–90.
14. B. E. Paton, S. V. Akhonin, and V. A. Berezos: In *Proceedings of the 13th World Conference on Titanium*, Wiley Online Library: 2016, pp. 359–64.
15. H.V. Zhuk, P.A. Kobryn, and S.L. Semiatin: *J. Mater. Process. Technol.*, 2007, vol. 190, pp. 387–92.
16. H.R. Harker: *Vacuum*, 1990, vol. 41, pp. 2154–56.
17. X. Zhao, C. Reilly, L. Yao, D.M. Maijer, S.L. Cockcroft, and J. Zhu: *Appl. Math. Model.*, 2014, vol. 38, pp. 3607–23.
18. Xu. Yaoping, C. Qipeng, L. Yuan, S. Yaming, Q. Tiechang, and S. Houfa: *Rare Metal Mater. Eng.*, 2020, vol. 49, pp. 3761–68.
19. L. Gao, H.-G. Huang, C. Kratzsch, H.-M. Zhang, K. Chattopadhyay, Y.-H. Jiang, and R. Zhou: *Int. J. Heat Mass Transf.*, 2020, vol. 147, p. 118976.
20. J.P. Bellot, D. Ablitzer, B. Foster, A. Mitchell, S. Hans, and E. Hess: *Metall. Mater. Trans. B*, 1997, vol. 28B, pp. 1001–10.
21. A. Mitchell: *Mater. Sci. Eng. A*, 1998, vol. 243, pp. 257–62.
22. M.J. Blackburn and D.R. Malley: *Mater. Des.*, 1993, vol. 14, pp. 19–27.
23. B.P. Bewlay and M.F.X. Gigliotti: *Acta Mater.*, 1997, vol. 45, pp. 357–70.
24. H. Mizukami, T. Kitaura, and Y. Shirai: In *MATEC Web of Conferences*, EDP Sciences: 2020, p. 10005.
25. G. Ghazal, P. Chapelle, A. Jardy, J. Jourdan, and Y. Millet: *ISIJ Int.*, 2012, vol. 52, pp. 1–9.
26. J.P. Bellot, D. Ablitzer, and E. Hess: *Metall. Mater. Trans. B*, 2000, vol. 31B, pp. 845–54.
27. Y. M. Zhang, H. Pfeifer, B. Friedrich, and L. Zhou: Trans Tech Publ. In *Materials Science Forum*, 2009, pp. 93–96.
28. Y. Jin, Fu. Xiaosen Dong, C.C. Yang, Y. Li, and W. Wang: *Metals*, 2018, vol. 8, p. 611.
29. A. Mitchell: *Mater. Sci. Eng. A*, 1999, vol. 263, pp. 217–23.
30. J.-P. Bellot, V. Descotes, and A. Jardy: *JOM*, 2013, vol. 65, pp. 1164–72.
31. C. Liu, S. Yang, J. Li, L. Zhu, and X. Li: *Metall. Mater. Trans. B*, 2016, vol. 47B, pp. 1882–92.
32. K. Peng, J. Wang, Q. Li, C. Liu, and L. Zhang: *Metall. Mater. Trans. B*, 2023, vol. 54B, pp. 928–43.